Molecular structure of enzyme-synthesized amylose-like chimeric isomaltomegalosaccharides and their encapsulation of the sulfasalazine prodrug

Weeranuch Lang[1,2,*], Yoshiaki Yuguchi[3], Chun-Yao Ke[1,4], Ting-Wei Chang[5], Yuya Kumagai[2,6], Wilaiwan Kaenying[2,7], Takayoshi Tagami[2], Feng Li[1], Takuya Yamamoto[1], Kenji Tajima[1], Kenji Takahashi[8], Takuya Isono[1], Toshifumi Satoh[1,9], and Atsuo Kimura[2,*]

[1]Faculty of Engineering, Hokkaido University, Sapporo 060-8628, Japan
[2]Research Faculty of Agriculture, Hokkaido University, Sapporo 060-8589, Japan
[3]Faculty of Engineering, Osaka Electro-Communication University, Osaka, 572-8530, Japan
[4]Institute of Polymer Science and Engineering, National Taiwan University, Taipei 10617, Taiwan
[5]Department of Chemical Engineering, National Tsing Hua University, Hsinchu 30013, Taiwan
[6]Faculty of Fisheries Sciences, Hokkaido University, Hakodate 041-8611, Japan
[7]Bureau of Laboratory Quality Standards, Department of Medical Sciences, Ministry of Public Health, Nonthaburi, 11000, Thailand
[8]Faculty of Biological Science and Technology, Institute of Science and Engineering, Kanazawa University, Kanazawa 920-1192, Japan
[9]ICReDD List-PF, Hokkaido University, N21W10, Kita-ku, Sapporo 001-0021, Japan
[*]Corresponding author: weranuch@eng.hokudai.ac.jp (W. Lang) tel, +81-11-706-6605; kimura@agr.hokudai.ac.jp (A. Kimura) tel/fax, +81 11 706 3872.

Abbreviations

Cac, critical aggregation concentration; CD, cyclodextrin; CGTase, cyclodextrin glucanotransferase, DDase, dextran dextrinase; D-IMS-*n*/*m*/*r* (e.g., D-IMS-28.3/13/3), D-IMS with DPs of *n* and *r* for nonreducing and reducing α-(1→4)-segments, respectively, where *m* is the DP of the main chain α-(1→6)-segment; DP, average degree of polymerization; DSC, differential scanning calorimetry; FWHM, full width at half maximum; IMS, isomaltomegalosaccharide; MADLS, multi-angle dynamic light scattering; MW, average molecular weight; N-4S, nonreducing end α-(1→4)-segment; N-IMS-*n*/*m* (e.g., N-IMS-25/7), N-IMS with DPs of *n* and *m* for nonreducing α-(1→4)- and α-(1→6)-segments, respectively; R-4S, reducing end α-(1→4)-segment; SAXS, small angle X-ray scattering; S-IMS, IMS with single R-4S; SEC, size exclusion chromatography; SZ, sulfasalazine; WAXS, wide-angle X-ray scattering

Abstract

The glucoconjugation between linear chimeric α-(1→4)- and α-(1→6)-glucosidic segments exhibits functional properties throughout their structure. In this study, we enzymatically synthesized three new series of chimeric nonreducing isomaltomegalosaccharides (N-IMS-*n*/*m*), each featuring a constant *n*, α-(1→4)-segment (DP = 22–25) at the nonreducing terminal, and varying *m*, α-(1→6)-main chain lengths (DP = 7–53). The synthesized compounds—N-IMS-25/7, N-IMS-24/19, and N-IMS-22/53—were compared to amylose (DP = 28) and previous samples of N-IMS-15/35 and D-IMS-28.3/13/3. D-IMS refers to a sugar with double α-(1→4)-segments at both the nonreducing and reducing ends. The binding affinity to the aromatic prodrug sulfasalazine (SZ) was assessed using a phase-solubility assay, followed by freeze-thawing. Wide-angle X-ray scattering revealed B-type crystalline patterns in bulk, and the crystallinity generally reduced with the increasing α-(1→6) segment. Interestingly, the B-type crystal structure was maintained even after SZ encapsulation, in contrast to the more common transition to V-type crystals upon drug encapsulation. Multi-angle dynamic light scattering and small-angle X-ray scattering revealed an intricate solution-state morphology, both in the absence and presence of SZ. Glucoconjugation aids in maintaining structural organization and integrity, even after the incorporation of the large SZ molecule.

Keywords: amylose, cyclodextrin glucanotransferase, glycoconjugation, helical segment, inclusion complex, synchrotron X-ray

1. Introduction

Carbohydrates typically exhibit a single functional property, which can limit their utility in complex medical applications or in advancing food science research (Dıblan, Salum, Ulusal, & Erbay, 2024; Zhang et al., 2023). To address this limitation, the strategy of covalently linking two functional carbohydrates has gained significant attraction (Pluemsab, Sakairi, & Furuike, 2005). This approach effectively combines the unique advantages of each carbohydrate, such as enhanced solubility and stability and precise binding or controlled release capabilities. For example, through this conjugation, β-cyclodextrin-assisted polysaccharides have shown potential in developing more effective therapeutic agents by leveraging the combined strengths of both components (Sahu, Patra, & Swain, 2023).

In this context, the inclusion properties of cyclodextrin [CD, a cyclic-type α-(1→4)-gluco-oligosaccharide] and amylose [a helical-type α-(1→4)-gluco-polysaccharide] attract notable interest in terms of maximizing therapeutic efficacy by improving drug solubilization, stabilization, and bioavailability (Wintgens, Lorthioir, Dubot, Sébille, & Amiel, 2015). The α-(1→4)-linkage in the amylose chain promotes helix formation, which is stabilized by hydrogen bonds mainly between the hydroxyl groups on carbon-2 and carbon-3 of glucose units in neighboring turns of the helix (Imberty,

De Recherche, & Perez, 1988). Specifically, amylose forms a left-handed helix, known as V-amylose, with the helix size determined by the complexing agent, typically resulting in structures containing six to eight glucosyl units per turn. In contrast, the cavity of CD is rigid, consisting of a single turn, and its structure is stabilized by hydrogen bonds formed between the hydroxyl groups on carbon-3 and the ring oxygen at carbon-5 of adjacent glucose units, contributing to its distinct toroidal shape.

The unique retrogradation property of amylose provides a straightforward approach for thermodenaturation and annealing with ligands, leading to the formation of a complex precipitate that can be easily isolated by centrifugation (Yang et al., 2013). Amylose is also easily digested by salivary and pancreatic α-amylases. However, forming complexes with drugs in a solvent-free environment poses challenges because of the propensity of amylose to form a double-helical structure with a parallel arrangement of chains, which leads to precipitation in water (Naknean & Meenune, 2010). In the solid or crystalline state, amylose can form crystalline regions as its molecules align in a consistent and repeating pattern. This organization leads to the development of polymorphic forms such as A-type and B-type crystals. A-type crystals are characterized by monoclinic unit cells packed with four water molecules per unit cell, while B-type crystals are characterized by water molecules centrally located within a six-double-helix structure, forming a hexagonal unit with 36 water molecules per unit cell. This compact helical arrangement renders the crystalline forms less soluble in water (Imberty et al., 1988; Surenchildren, Mohanty, Liu, & Misra, 2022).

In contrast, backbone α-gluco-polysaccharides, such as dextran, which is a linear α-(1→6)-glycosidic chain, do not have the capacity to form inclusion complexes, but possess excellent solubility and customizable properties (Hu, Lu, & Luo, 2021; Sundari & Balasubramanian, 1997). CD and dextran conjugates are commonly synthesized using chemical methods (Nielsen, 2010; Ramirez et al., 2007). Furthermore, amylose engineering *via* chemoenzymatic synthesis produces amylose-block polymers, amylose-graft polymers, amylose-modified surfaces, and cellodextrin hybrids (Nishimura & Akiyoshi, 2017). However, to the best of our knowledge, the synthesis of amylose-grafted dextran has not yet been reported by other research teams. In our previous work, we synthesized amylose-grafted dextran using two distinct enzymatic methods to explore the structural interplay of these systems. Building on this, the present study further investigates how the α-(1→4)- and α-(1→6)-linked segments influence the overall crystalline pattern of the system during complexation with hydrophobic drugs. *Gluconobacter oxydans* ATCC 11894 dextran dextrinase (DDase, EC 2.4.1.2) can synthesize water-soluble α-(1→6)-dextran containing small amount of α-(1→4)-linkage from maltodextrin. The appearance of shorter chimeric isomaltomegalosaccharide (IMS) intermediates, which precede dextran, suggests that the reducing terminal α-(1→4)-segment (R-4S) is derived from maltodextrin, maintaining the α-anomeric configuration of the substrates in the end products (Lang et al., 2022a; Sadahiro et al., 2015; Yamamoto, Yoshikawa, & Okada, 1993). The conjugation of this single short chimeric R-4S α-(1→4)- and α-(1→6)-glucosidic segments by

DDase, defined the name as S-IMS, retains its functional property (Hara, Kume, Iizuka, Fujimoto, & Kimura, 2017; Lang et al., 2014; Lang et al., 2022b; Shinoki et al., 2013). S-IMS also serves as an acceptor substrate for *Bacillus macerans* cyclodextrin glucanotransferase (CGTase; EC 2.4.1.19) coupling reaction. The resulting D-IMS-28.3/13/3 bearing amylose-like helical nonreducing end α-(1→4)-segment (N-4S) with an average degree of polymerization (DP) of 28.3 displayed a water-soluble complex with aromatic drugs (Lang et al., 2023a). We proposed a size-dependent nomenclature for D-IMS-*n*/*m*/*r*, where *n*, *m*, and *r* represent DPs of N-4S, α-(1→6)-segment, and R-4S, respectively (Scheme 1).

Recently, we enzymatically synthesized amylose-like helical nonreducing chimeric IMS (N-IMS), featuring α-(1→6)-dextran as the main chain, as opposed to S-IMS, with N-4S serving as an anchor portion (Lang et al., 2023b). The N-4S, with DP of 15, was derived from α-CD donor substrate elongation toward the α-(1→6)-main chain of partially purified dextran brand T 10 acceptor substrate by CGTase. This helical N-4S demonstrated a significant inclusion ability, enhancing the aqueous solubility of lipophilic azobenzene dyes. These findings suggest that the cylindrical cavity of N-IMS encapsulates the aniline molecule with 2.14 helical turns. The term "N-IMS-15/35" introduced in this study and Scheme 1b illustrates this concept.

As indicated, N-IMS-15/35 improved the spontaneous digestion of model lipophilic pollutant dyes through coupled azoreductase and glucose dehydrogenase in simulated biological treatments without organic solvents, making it a safe and gentle approach for biological applications (Lang et al., 2013; Lang et al., 2023b). Conjugation with dextran suggests that the amylose-like helical N-4S is less likely to decrease an aggregate double helix, and this modulation has been distinctly observed from a molecular viewpoint. Despite this progress, the specific factors affecting drug encapsulation and molecular conformation in these systems remain unclear. Therefore, this study focuses on understanding the structural interactions between the N-4S α-(1→4)-segment and the α-(1→6)-segment, particularly in the formation of N-IMS complexes with a large hydrophobic drug. Sulfasalazine (SZ) is an anti-inflammatory azo drug that targets delivery to the colon and is used to treat inflammatory bowel disease and rheumatoid arthritis. The drug is intended for long-term treatment but has adverse effects (e.g., gastric distress and headache) and may interact with some components, such as folic acid, taken orally (Situnayake & McConkey, 1986; Grindulis & McConkey, 1985). The major advantage of the coated carrier is that it reduces the total dosage and the possible harmful consequences of free drugs to other organs.

In this study, we synthesized three new series of N-IMS with varying lengths of α-(1→6)-segment, formed from dextran DP 10, 20, and 59. Concurrently, we clarified the molecular structures of N-IMS, N-IMS-15/35, D-IMS-28.3/13/3, and commercial amylose with a DP of 28. The pure sugars and SZ-loaded complexes in their solid states were characterized using wide-angle X-ray scattering (WAXS). Furthermore, their conformations in solution were analyzed using multi-angle

dynamic light scattering (MADLS) and small-angle X-ray scattering (SAXS). For the first time, we have elucidated the structural framework of a novel glucoconjugation between amylose and dextran.

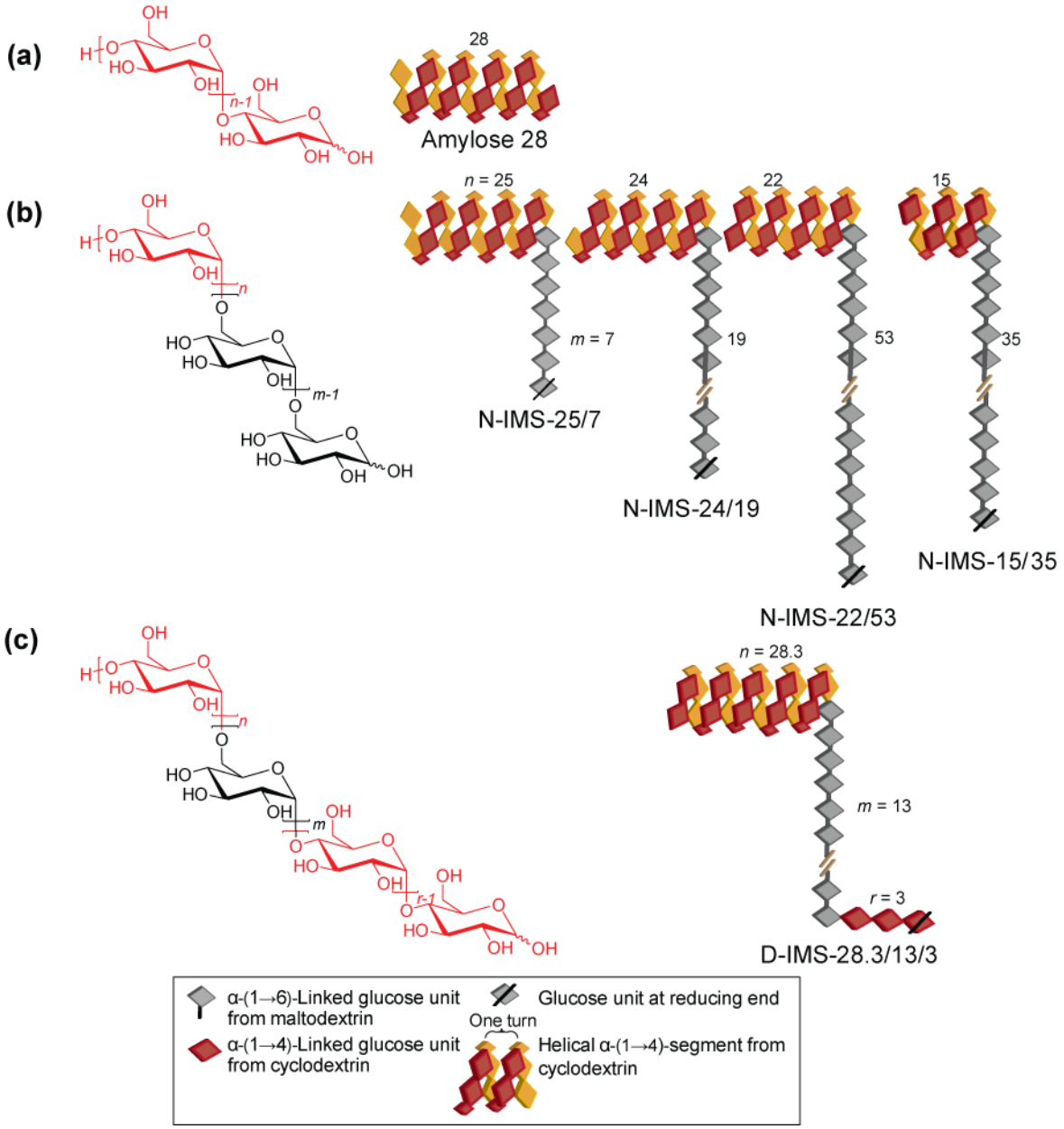

Scheme 1. (a) Short amylose with DP of 28. (b) N-IMS-*n*/*m*, where N-4S represents *n* units of the α-(1→4)-linked segment coupled to the non-reducing end of an α-(1→6)-glucosyl main chain containing *m* units. The *n* and *m* indicate DP of N-4S and α-(1→6)-segment, respectively: IMS-25/7, N-IMS-24/19, and N-IMS-22/53. N-IMS-15/35 is referenced from Lang et al. (2023b). (c) D-IMS-*n*/*m*/*r*, with DPs of *n* and *r* for the nonreducing and reducing α-(1→4)-segments, respectively, and *m* representing the DP of the α-(1→6)-segment main chain. The D-IMS-28.3/13/3 model is modified from our previous data (Lang et al., 2023a).

2. Materials and methods

2.1. Materials. SZ was purchased from Sigma-Aldrich (St. Louis, MO, USA). Synthetic amylose with a molecular weight of 4.5 kDa (DP 28), was obtained from Glico Nutrition (Osaka, Japan) and was subjected to WAXS analysis without any additional processing. Dextran T 1.5 (DP = 10) and T 3.5 (DP = 20) were obtained from Pharmacosmos (Holbaek, Denmark) where T 10 (DP = 59) was purchased from Amersham Biosciences (Uppsala, Sweden) and used without further purification. α-CD (Nihon Shokuhin Kako, Tokyo, Japan) and CGTase (liquid form containing 13.8 ± 2.5 U/mL, Amano Enzyme, Nagoya, Japan) were kindly donated. N-IMS-15/35 was obtained as previously described (Lang et al., 2023b). Size exclusion chromatography (SEC) external standards for P-82 pullulans (P-5, P-10, P-20, P-50, P-100, P-200, P-400, and P-800) and maltoheptaose were obtained from Showa Denko K.K. (Kanagawa, Japan) and Nihon Shokuhin Kako (Tokyo, Japan), respectively. Dimethyl sulfoxide (DMSO) and other chemicals were purchased from Nacalai Tesque (Kyoto, Japan).

2.2. N-IMS production and characterization. A series of N-IMSs was synthesized following previous methods (Kimura, Hara, & Lang, 2015; Lang et al., 2023b), with the addition of a broader range of commercial dextran products. Three dextran T series (T 1.5, T 3.5, and T 10, at 20 mM) were dissolved in water with α-CD (100 mM) and incubated with CGTase (0.14 U/mL) at 20 ℃ for 3 h. The resulting products were purified using the same methods (precipitation in methanol, removal of residual methanol by evaporation, redissolution in water, freezing, and lyophilization) (Lang et al., 2023b). The linkage composition and DP were determined by ^{1}H NMR, and the results indicated that N-IMS-25/7, N-IMS-24/19, and N-IMS-22/53 were produced from dextran at T 1.5, T 3.5, and T 10, respectively. SEC was performed using a high-performance liquid chromatography system with two columns connected in series: 8.0×300 mm Shodex OHpak SB-803 HQ (separation size, 1–100 kDa) and 8.0×300 mm SB-806 HQ (separation size, 100–20000 kDa). Elution was carried out using 0.1 M sodium nitrate at a flow rate of 0.5 mL/min and 40 °C. The detection was performed using a refractive index detector (RI 2031 Plus; JASCO, Tokyo, Japan). Calibration was performed using Shodex standards, P-82 pullulans, and maltoheptaose. Water solubility was determined using a previously described method (Lang et al., 2022b).

2.3. Complex formation with SZ. Given the distinct water solubility characteristics of each sample (Table 1), water-soluble complexes were created using an excess of SZ (10 g/L) with the same weight of 200 mg for all samples. The concentrations were set to 20, 25, 40, 100, 100, and 25 g/L for amylose DP 28, N-IMS-25/7, N-IMS-24/19, N-IMS-22/53, N-IMS-15/35, and D-IMS-28.3/13/3, respectively. These concentrations ensured full solubility in deionized water following preboiling with brief microwave heating. The complexes were then incubated at 37 °C and shaken at 100 rpm in a water-bath shaker (Yamato Scientific BT 100, Tokyo, Japan) for 3 h, and subsequently cooled down to

25 °C for 30 min. Water was used as the control for each sample. Using method "S," the solution phase was filtered using a sintered-glass funnel. Post-dilution with DMSO, the SZ concentration in the supernatant was measured at 374 nm, and calculations were performed using a calibration curve to ascertain C_0 and C, which denote the SZ concentrations (μM) in water (free SZ) and in the complexes, respectively. The dry mass (M, g) of all the samples in the supernatant was determined after lyophilization. The SZ-binding capacity of the soluble complex (q_S, mg/g) was calculated using Equation (1):

$$q_S = \frac{(C-C_0)MW_{SZ}V}{1000M} \quad (1)$$

where MW_{SZ} is the molecular weight (398.39 g/mol). V is 0.01, 0.008, 0.005, 0.002, 0.002, and 0.008 L for amylose DP 28, N-IMS-25/7, N-IMS-24/19, N-IMS-22/53, N-IMS-15/35, and D-IMS-28.3/13/3, respectively.

For method "C," the dried complexes obtained from method "S" were suspended with 1 mL water and frozen at –80 °C for 3 h, thawed at 4 °C for overnight to induce nucleation (Pfannemüller, 1987), and subsequently centrifuged (12,000 ×g, 10 min, 4 °C) to discard the supernatant including the free SZ. The insoluble fraction was then freeze-dried. The drug loading in each dried component was analyzed by dissolving 5 mg of the dried powder in 1 mL of DMSO. Trapped SZ was measured at 374 nm using a calibration curve. The binding capacity for SZ obtained from the insoluble complex (q_C, mg/g) was calculated using Equation (2), where M = 0.005 g and V = 0.001 L:

$$q_C = \frac{CMW_{SZ}V}{1000M} \quad (2)$$

2.4. Complex characterization in bulk

2.4.1. Fourier Transform infrared (FT-IR). FT-IR analysis was conducted using a PerkinElmer Frontier MIR spectrometer (Waltham, MA, US) equipped with a single-reflection diamond ATR (attenuated total reflection) accessory. The spectra were recorded from 500 to 4000 cm^{-1}.

2.4.2. WAXS. WAXS experiments on bulk samples were performed at the BL-6A beamline of the Photon Factory, High Energy Acceleration Research Organization (Tsukuba, Japan), where the X-ray wavelength and exposure time were 0.150 nm and 60 s, respectively. A PILATUS3 100 K (Dectris, Switzerland, 487×195 pixels, 172×172 μm pixel size) detector was used for data acquisition. The sample-to-detector distance was 300 mm and was calibrated using the scattering pattern of silver behenate. The collected data of $I(q)$ versus q (nm^{-1}) was corrected by subtracting the signal from the Kapton blank, as the powder samples were sandwiched between Kapton films during measurement, and normalized by dividing the intensities by the incident beam intensity to account for fluctuations in the X-ray source.

Bragg's Law, $n\lambda = 2d\sin(\theta)$, defines that for the first diffraction order (n = 1), the interplanar spacing (d) simplifies to $d = \lambda/\sin(\theta)$. With the X-ray wavelength (λ) typically at 0.154 nm for Cu Kα radiation, the Bragg angle (θ) can be converted to radians using the formula θ (radians) = θ(degrees) × π/180. The q-value relates to d-spacing with an inverse relationship given by $d = 2\pi/q$. Amylose A-type crystals exhibit strong diffraction peaks at 2θ (λ = 0.154 nm) values of 15°, 17°, 18°, and 23°, corresponding to q-values of 10.92, 12.37, 13.09, and 16.69 nm^{-1}, respectively (Sun et al., 2021). An example of the calculation: for Cu Kα 2θ = 17°, θ (radians) = (8.5 × 3.14) / 180 = 0.15, then q = 4πsin(0.15) / 0.154, resulting in a q-value of approximately 12.05 nm^{-1}, yielding a d-spacing of 0.52 nm. Using similar calculations, amylose B-type crystals displayed peaks at 5.7°, 17°, 20°, 22°, and 24°, with the strongest peaks at 5.7°, 17°, 22°, and 24° (Bertoft, 2017; Frost, Kaminski, Kirwan, Lascaris, & Shanks, 2009), corresponding to q-values of 4.05, 12.05, 15.55, and 16.95 nm^{-1}, respectively. The degree of crystallinity (%W_c) was determined by peak deconvolution using PeakFit version 4, integrating the areas under the crystalline peaks and the total scattering area. The degree of crystallinity is expressed using Equation (3):

$$\%W_c = \left(1 - \frac{A_a - A_{af\,Dex}}{A_{total} - A_{af\,Dex}}\right) \times 100 \qquad (3)$$

where A_a is the area of the broad amorphous halo, encompassing the sum of $A_{a\cdot N\text{-}4S}$ and $A_{a\cdot Dex}$, which represent the α-(1→6)-main chain. A_{total} is the area of the entire diffraction pattern. f_{Dex} is the weight fraction of the α-(1→6)-linkage, inferred from the α-(1→4)-linkage content percentage in Table 1: f_{Dex} = 0, 0.231, 0.444, 0.708, 0.710, and 0.300 for amylose 28, N-IMS-25/7, N-IMS-24/19, N-IMS-22/53, N-IMS-15/35, and D-IMS-28.3/13/3, respectively.

The crystallite size was determined using the Scherrer equation, $L = K\lambda/\beta\cos(\theta)$, where L is the average crystallite size, K is the shape factor (taken as 1, as reported by Zitting, Paajanen, & Penttilä, 2023), λ is the X-ray wavelength (0.154 nm), β is the FWHM of the diffraction peak, and θ is the Bragg angle. In reciprocal space (where $q = 4\pi\sin(\theta)/\lambda$), the equation can be expressed by equation (4):

$$L = \frac{2\pi K}{\Delta q} \qquad (4)$$

Here, the broadening of the diffraction peak, Δq, in reciprocal space is described by integral breadth.

2.5. Complex characterization in solution

2.5.1. MADLS. MADLS analyses were performed using the ELSZneo instrument (Otsuka Electronics, Tokyo, Japan) on aqueous solutions of pure sugar and complex "C" samples (see section 2.3). Each 2 mL sample (5 g/L) was heated to 100 °C for pure sugar or 80 °C for complexes for 10 min before centrifugation. Scattering angles of 46°, 90°, and 165° were used sequentially, conducting 25 runs at each angle for three cycles at 25 °C. The hydrodynamic radius (R_h) was calculated from the DLS autocorrelation functions using cumulant analysis software.

2.5.2. SAXS. All samples were dissolved in Milli-Q water, and their complexes "S" and "C" were prepared following sections 2.3 and 2.5.1, then stored at 25 °C for two weeks prior to measurement. SAXS measurements were performed using the BL-6A beamline of the Photon Factory, High Energy Acceleration Research Organization (Tsukuba, Japan). Guinier analysis and Kratky plots were conducted, where the radius of gyration (R_g, nm) values were calculated manually, following the method outlined by Lang et al. (2023a). The SAXS curve is represented as log $I(q)$ versus log q, where $I(q)$ is the scattering intensity and q is the magnitude of the scattering vector.

3. Results and discussion

3.1. Synthesis and characterization of N-IMS-*P*/*Q*. Three N-IMS compounds of varying sizes (N-IMS-25/7, N-IMS-24/19, and N-IMS-22/53) were synthesized according to the protocol established for N-IMS-15/35 in a previous study (Lang et al., 2023b), with a focus on the acceptor lengths of dextran T 1.5 (DP 10), T 3.5 (DP 20), and dextran T 10 (DP 59). The molar ratio of α-CD to acceptor dextran was set at 5:1, theoretically predicting $n = 30$ for the N-4S segments. However, the N-4S chain length in the obtained products was 22–25, which was shorter than the expected $n = 30$. This could be a result from the cyclization mode of CGTase, which cleaves long α-(1→4)-linkages to produce α- or β-CD, or due to minor hydrolysis activity on α-(1→4)-glycosidic bonds (Lang et al., 2023a). We also found that the *m* length was slightly shorter than that of the acceptor, dextran. The discrepancy in *m* length may be attributed to the lower specificity of CGTase for the long acceptor length. The ^{1}H NMR spectra depicted in Fig. 1a reveal the predominant peaks corresponding to α-(1→4)- and α-(1→6)-glucosidic linkages. The percentages of α-(1→4)-linkage were estimated to be 76.9%, 55.6%, and 29.2%, respectively. Additionally, the peak molecular weights (M_p) determined by SEC were 4.1, 6.9, and 12.2 kDa, respectively (Table 1). SEC analysis revealed a single peak for each compound, with molecular weight dispersity from 1.7 to 1.9 (Fig. 1b).

N-IMS-25/7, with a total DP of 32, has a rich proportion of α-(1→4)-linkage, leading to increased precipitation tendency and reduced water solubility (104 g/L). N-IMS-24/19, with a total DP of 43, displays a more balanced mix of α-(1→4)- and α-(1→6)-linkages, achieving moderate solubility (164 g/L). N-IMS-22/53, with a total DP of 75, has the highest content of α-(1→6)-linkage, which significantly enhances its solubility (> 400 g/L). N-IMS-22/53, sharing the dextran T 10 acceptor with N-IMS-15/35, is analogous in possessing a longer α-(1→6)- and α-(1→4)-glucose chains. The overall results indicate that the enhancement of hydrophilicity through α-(1→6)-linkages, which reduced aggregation and improved water dispersion, aligns with previously reported findings (Lang et al., 2023a). Additionally, the pronounced absorbance pattern from iodine staining suggests the inclusion ability stems from α-(1→4)-linkages within the chain, as the donor-substrate α-CD lacks this capability (Fig. 1c). This method is widely used to assess the amylose content of starch

quantitatively (Bertoft, 2017; Breitinger, 2003). The linkage composition, DP, yield, and overall properties of the three N-IMS compounds are outlined in Table 1, along with comparisons with amylose 28, N-IMS-15/35, and D-IMS-28.3/13/3.

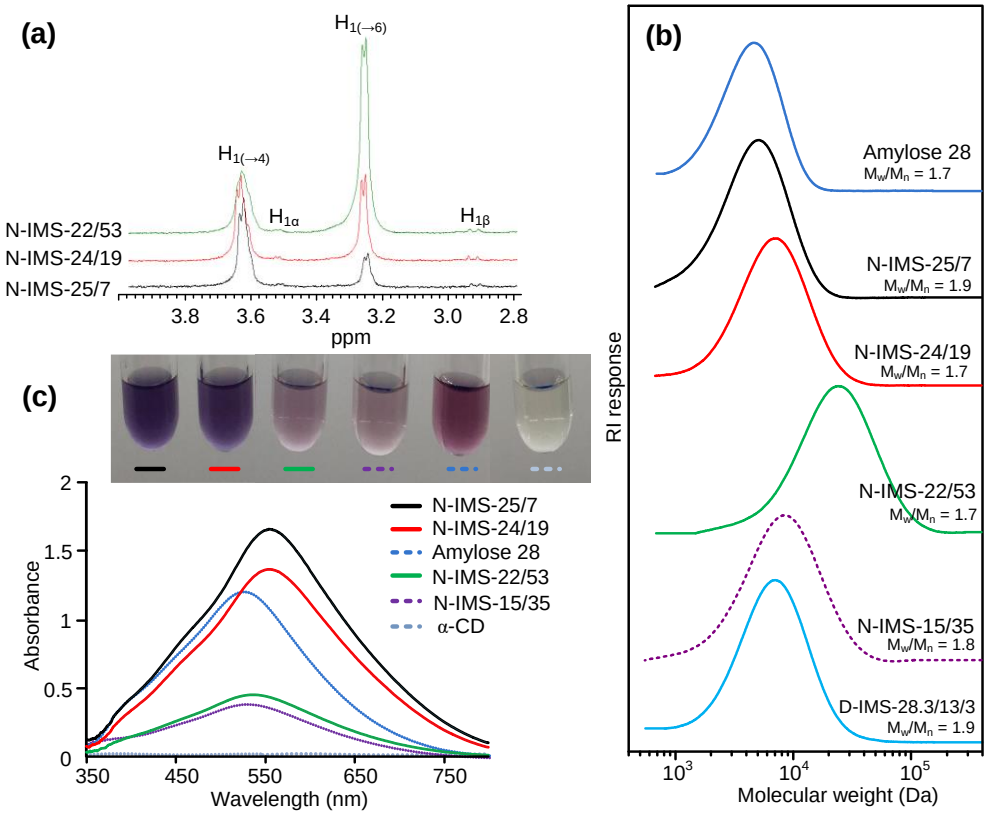

Fig. 1. (a) Partial ^{1}H-NMR spectra (400 MHz, 40%, v/v, DMSO-d_6/D_2O at 60 °C) of the newly synthesized compounds N-IMS-25/7, N-IMS-24/19, and N-IMS-22/53. (b) SEC trace of six pure sugar samples utilized in this study. M_w/M_n is a molecular weight dispersity. (c) Visible spectra of iodine-stained N-IMS-25/7, N-IMS-24/19, N-IMS-22/53, N-IMS-15/35, amylose with DP of 28, and α-CD (0.5 g/L). The inset displays the coloration resulting from the iodine staining. Notably, the data for D-IMS-28.3/13/3 is not presented here, as it is available elsewhere (Lang et al., 2023a).

Table 1. Characterization of the sugar samples used in this study.

N-IMS-*n*/*m* or DMS-*n*/*m*/*r*	Amylose 28	N-IMS-25/7	N-IMS-24/19	N-IMS-22/53	N-IMS-15/35	D-IMS-28.3/13/3
Acceptor substrate	N/A	T 1	T 3.5	T 10	T 10	S-IMS-0/13/3
Content of α-(1→4)-linkage (%)	100	76.9	55.6	29.2	29.0	70.0
Yield (%, w/w)	N/A	90	85	50	55	80
DP of N-4S	28	7	24	22	15	28.3
Molecular mass [a] (kDa)	4.5	4.1	6.9	12.1	8.1	7.2
Solubility (g/L)	10.5 [b]	104	164	> 400	> 400	80

[a] Peak molecular weight (M_p) determined by SEC

[b] The value obtained from Lang et al. (2022b).

N/A = Not available

N.D. = Not determined.

3.3. Crystalline structure of chimeric sugars. In our previous study, XRD analysis showed that amylose 28 and D-IMS-28.3/13/3 displayed a B-pattern, which further transitioned to a Vh-7 structure, wherein one helix turn comprised seven glucosyl units after encapsulation in ibuprofen (Lang et al., 2023a). B-type crystals possess a hexagonal unit cell with more widely spaced helices, which allows for greater water content and hydration. In contrast, A-type crystals have monoclinic unit cells and feature densely packed double helices, leading to reduced water content and solubility (Bertoft, 2017; Surenchildren et al., 2022). In this study, we used WAXS to examine the crystalline structures of amylose and chimeric sugars across the q range of 7.2–18.8 nm^{-1}. Fig. 2a displays the characteristic diffraction peaks in the WAXS patterns, revealing crystallization in all sugar samples. The sharp peaks at q values of 11.97, 15.97, and 16.76 nm^{-1} correspond to d-spacings of 0.52, 0.40, and 0.37 nm, respectively (see Section 2.4.2). These align with the diffraction peaks of B-type amylose crystals at 2θ (λ = 0.154 nm) of 5.7° (d-spacings of 1.55 nm), 17° (d-spacings of 0.52 nm), 22° (0.40 nm), and 24° (0.37 nm) (Bertoft, 2017).

The B-type crystal diffraction pattern was distinct in commercial amylose 28, with a degree of crystallinity (%W_c) of 32.7% (Table 2), which agrees with our previously mentioned XRD pattern (Lang et al., 2023a). N-IMS-25/7, N-IMS-24/19, and D-IMS-28.3/13/3 also exhibited a B-type crystal diffraction pattern (Fig. 2) at a similar %W_c level (34.2% – 41.0%) (Table 2). This aligns with Pfannemüller's (1987) finding that amylose chains form B-type crystals when the DP is 13 or higher, whereas malto-oligosaccharides with a DP of 10–12 form A-type crystals and those with a DP below 10 do not crystallize. Therefore, the short α-(1→6)-chains in these samples (n = 7, 19, and 13 glucosyl units, respectively) did not interfere significantly with N-4S's ability to form double helices.

In contrast, the WAXS profiles of N-IMS-22/53 and N-IMS-15/35 exhibit broad halos, indicating their less crystalline nature. This suggests that the longer α-(1→6)-linkages (n = 53 and 35 glucosyl units) may subtly disrupt the crystallization ability of the α-(1→4)-chains, resulting in the low %W_c level of 19.9% for N-IMS-22/53 and 19.1% for N-IMS-15/35 (Table 2). According to Scherrer's equation, the diffraction peak width is inversely proportional to the crystallite size. As inferred from the broad peak of N-IMS-22/53, the crystallite size was estimated to be 2.85 nm. In contrast, sharper peaks reflected larger crystallites, with the largest size (5.46 nm) observed for N-IMS-24/19 among the chimeric sugars.

Table 2. Crystallinity degree (%W_c) and crystallite size of sugar samples and their complexes with sulfasalazine (SZ).

Sample	%W_c		Δq of 17° peak		Crystallite size (nm)	
	Without SZ	With SZ	Without SZ	With SZ	Without SZ	With SZ
Amylose 28	32.7	N/A	1.126	N/A	5.58	N/A

N-IMS-25/7	41.0	59.6	1.313	1.315	4.78	4.78
N-IMS-24/19	34.2	41.6	1.151	1.317	5.46	4.77
N-IMS-22/53	19.9	29.1	2.205	2.036	2.85	3.08
N-IMS-15/35	19.1	43.7	1.424	1.575	4.41	3.99
D-IMS-13.3/13/3	37.8	73.0	1.085	1.128	5.79	5.57

N/A = Not available due to baseline inconsistencies in the WAXS measurement.

[a] Integral breadth.

[b] Calculation method described in Section 2.4.2.

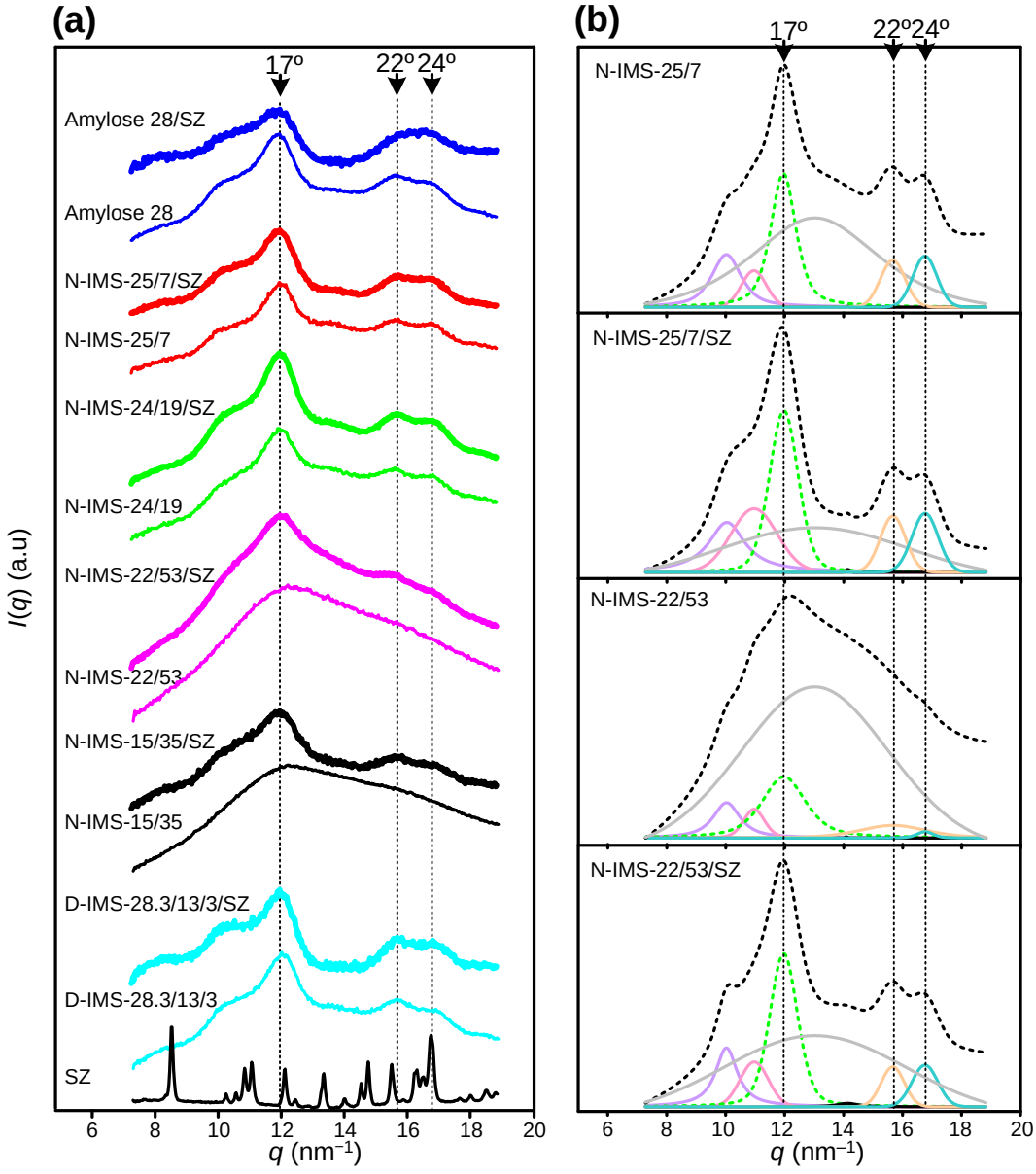

Fig. 2. WAXS profiles (a) of six sugar samples (thin lines) and post-encapsulation with sulfasalazine (SZ) (thick lines), shown as intensity $I(q)$ versus q. Arrows indicate peak positions corresponding to 2θ ($\lambda = 0.154$ nm) values of 17°, 22°, and 24°. Peak deconvolution (b) for N-IMS-25/7, N-IMS-22/53,

and their SZ complexes is presented. Solid peaks represent crystalline regions, while black- and gray lines indicate the PeakFit software-generated fits and the total amorphous peaks, respectively. Full deconvolutions for all samples (except amylose 28/SZ) are available in Fig. S3.

3.4. Binding capacity to SZ. In this study, we investigated two approaches for complexing SZ without employing organic solvents, particularly DMSO, urea, or alkaline solutions, which are commonly used for polysaccharide dissolution (Bertoft, 2017). Method "S" is a traditional approach developed to study the solubility enhancement of drugs with poor water solubility by increasing the concentration of a solubilizing agent (Higuchi & Connors, 1965). This method is widely used in pharmaceutical sciences. Using this method, any excess water-insoluble drug that does not form complex precipitates can be separated by centrifugation or filtration. The phase solubility diagram displays the total dissolved drug in both the complex and free states, with the latter indicating the intrinsic water solubility of the drug. Fig. 3a provides a concise overview of the workflow for drug complex preparation and analysis, further summarizing key findings at each stage of the analysis.

In detail, microwave heating was utilized to achieve the high temperatures necessary for the complete dissolution of the pure sugars. In method "S," phase solubility takes into account both complexed SZ and free SZ (28 μM), although the q_S calculation can subtract the amount of free drug (equation 1, Section 2.3). It should be noted that the samples are further characterized with SAXS in Section 2.5.2, as mentioned in the context of the complex "S," containing a measurable amount of the free drug. A high q_S value indicates a qualified soluble complex, as demonstrated by N-IMS-25/7 (3.8 ± 0.1 mg/g) and N-IMS-24/19 (2.6 ± 0.0 mg/g). Conversely, samples with low α-(1→4)-chain content, such as N-IMS-22/53 (1.5 ± 0.0 mg/g) and N-IMS-15/35 (0.4 ± 0.0 mg/g), were slightly ineffective in encapsulating the drug, resulting in a lower binding capacity (Fig. 3b). D-IMS-28/13/3, distinguished by its main chain with the α-(1→6)-linkage and a short chain of 2–3 units of α-(1→4)-glucose at the reducing end, has a moderate q_S value (2.5 ± 0.2 mg/g) that falls between N-IMS-24/19 and N-IMS-22/53.

Method "C" is more effective in eliminating free drug when the complexed drug can be precipitated through the heating/annealing process of amylose by retrogradation (the term described that gelatinized starch reassociates and precipitates upon cooling) (Lang et al., 2023a; Yang et al., 2013). Complexes prone to high aggregation may exhibit similar q_S and q_C values, with q_C being significantly lower than q_S if they are less aggregated in water. Amylose 28 demonstrates this, showing equal q_S (0.8 ± 0.0 mg/g) and q_C (0.7 ± 0.2 mg/g) values (Fig. 2). However, N-IMS-25/7 exhibited a greater q_C binding capacity that was 2-fold higher (2.1 ± 0.2 mg/g). Therefore, it could act as a more efficient drug coating comparable to amylose 28 and safer than using the method approached by Wang et al. (2021), preparing amylose and drug complex, e.g., catechin, in DMSO at 90 °C.

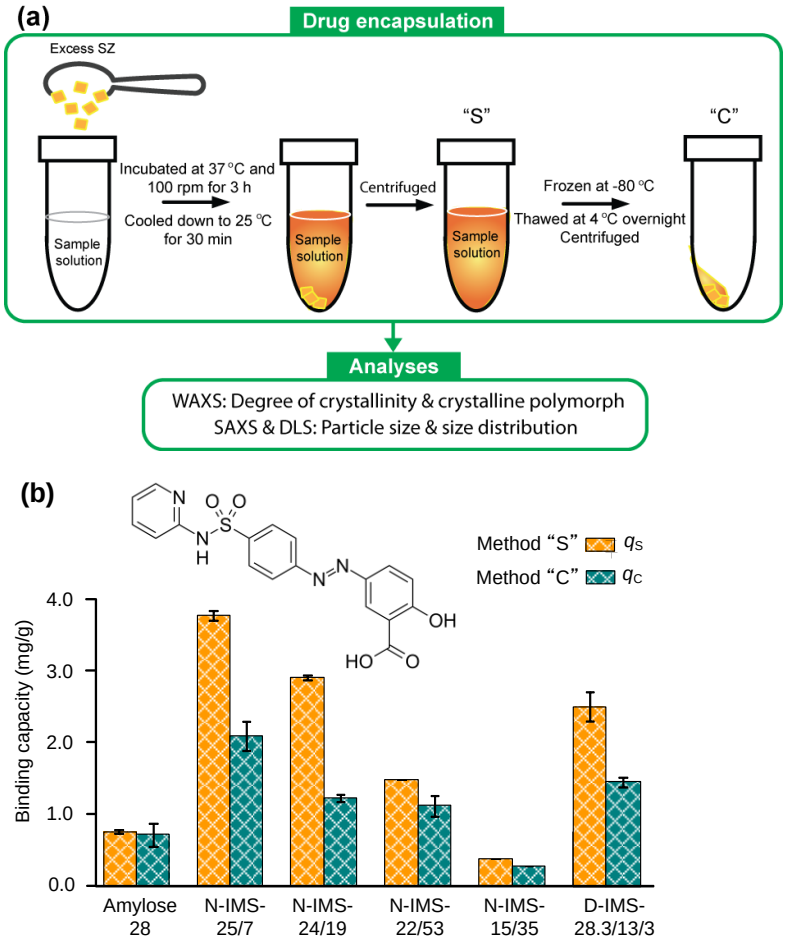

Fig. 3. (a) Overview of the workflow for drug complex preparation and analysis, highlighting the key findings at each step. (b) Binding capacities of six sugars for the SZ drug analyzed using two sequential methods, "S" and "C".

3.5. Crystalline property post-encapsulation. Before encapsulation, the samples exhibited B-type crystals, characterized by double helices in a hexagonal unit cell, indicating a high-water content and less dense packing compared with that of the A-type structure. Post-encapsulation, WAXS confirmed that B-type crystalline structures persisted, with characteristic peaks at 2θ angles corresponding to *d*-spacings of 0.52, 0.40, and 0.37 nm (q = 11.97, 15.97, and 16.76 nm^{-1}), though with altered sharpness (Fig. 2a). Changes in the $\%W_c$ level after drug encapsulation are summarized in Table 2. The peak at 17° (*d*-spacing = 0.52 nm), indicating the spacing between the double helices, was retained, indicating a stable B-type structure. The disappearance of this peak under high hydrostatic pressure suggests the possible disruption and transition to a more amorphous state, that is, gelatinization (Yang et al., 2016).

Notably, all chimeric sugars exhibited a significantly higher $\%W_c$ level after drug encapsulation, suggesting that the B-type crystalline arrangement was maintained or even enhanced. For example, the $\%W_c$ of N-IMS-24/19 increased from 34.2% to 41.6%. However, the crystallite

sizes for N-IMS-24/19, N-IMS-15/35, and D-IMS-28.3/13/3 decreased, such as from 5.46 nm to 4.77 nm for N-IMS-24/19 (Table 2). The increasing trend of %W_c as the crystallite size decreased suggests that the drug molecules acted as nucleating agents, leading to the formation of multiple small crystallites.

Interestingly, both N-IMS-22/53 and N-IMS-15/35 exhibited improved B-type crystalline diffraction patterns after encapsulation, with N-IMS-22/53 exhibiting a well-defined pattern (Fig. 2a, b). Despite the potential steric hindrance from the dextran segments, these segments did not appear to disrupt the B-type crystal structure.

Notably, the FTIR results were inconclusive because of the minimal mass of the drug in the complexes (Fig. S1). Vh-7-type crystals were previously identified in amylose and D-IMS-28.3/13/3 after ibuprofen encapsulation (Lang et al., 2023a). The retention of the B-type structure in this study may be due to the relatively large size of SZ (1.26 nm), which is likely too long to be fully encapsulated within the single helix of the sugar samples, compared to ibuprofen (0.98 nm) (Fig. S2). This may be due to steric hindrance between SZ and β-CD, where SZ adopts an L-shaped conformation with the benzoic acid moiety entering β-CD, preventing the pyridine residue from complexing (Tahir, Cao, Azzouz, & Roy, 2021).

3.6. Structure analysis in water using MADLS. Carbohydrates in water can exist as single chains or higher-order structures, such as multiple-stranded helices or larger aggregates/precipitates, influenced by hydrogen bonding, which is a key noncovalent force driving both physical aggregation and self-assembly (Tao & Bernasek, 2005). DLS provides insights into how the molecular architecture affects self-assembly from a detailed particle-size distribution. The slow mode of DLS is often attributed to scattering from large aggregates or clusters of polymer chains. In addition, larger particles scatter light more intensely at smaller angles, while smaller particles scatter at larger angles (Lasemi, Rupprechter, Liedl, & Eder, 2021). For instance, Zhang, Li, and Zhang (2010) demonstrated that low molecular weight polysaccharide lentinan (approximately 500 kDa), which forms triple helix structure, exhibits a bimodal DLS size distribution, with R_h of 14.9 nm for individual single chains and 98.4 nm for triple helix.

The hydrodynamic properties of the samples and their complexes with SZ were evaluated by analyzing the autocorrelation function of the intensity fluctuations observed at three distinct detection angles (Fig. 4). Amylose 28, relevant to this study, consists of repeating glucosyl units linked by α-(1→4)-bonds, closely resembling the N-4S moiety of N-IMS and D-IMS samples. The conformation of amylose in neutral aqueous solutions can vary significantly, with interpretations ranging from disordered chains, random coils, and extended coils to worm-like helices or random coils with extended helical segments (Bertoft, 2017; Braga et al., 1985). In aqueous solutions, particularly in pure water, amylose is unstable and tends to form double helices that readily precipitate during

retrogradation. The initial exponential decay of the short amylose 28 is shown in Fig. 4a. At the detection angle of 46°, the intensity autocorrelation function G2(τ) curves exhibited a complex decay, indicating a range of different-sized particles or fluctuations in the particle sizes (Lasemi et al., 2021). The intensity-based size distributions shown in Fig. S4 show bimodal patterns at 46° and 90°, suggesting the presence of two distinct populations of particles. When converted into a number-averaged size distribution, a single peak at R_h = 1.4 nm was observed (Fig. S5, Table 3). As mentioned previously, larger particles scatter light more intensely, making them detectable even in small populations. This suggests that, while the majority of the sample is molecularly dissolved as a single molecule, a small fraction exists as aggregates with an R_h of approximately 65 nm. Upon complexation with SZ, the resulting number-based size distribution suggests a transition from a single molecular state to aggregates with an R_h value of 14.2 nm.

The autocorrelation functions of N-IMS-25/7 and N-IMS-24/19 exhibited similar decay patterns before and after SZ encapsulation (Fig. 4b–c). However, intensity-based size distributions (Fig. S4) show bimodal patterns at 46°, 90°, and 165°, indicating the presence of two distinct particle size populations. The number-based R_h reveals a slight increase for N-IMS-25/7, growing from 21.6 to 25.2 nm after encapsulation (Table 3). This indicates that N-IMS-25/7 had already formed aggregates before encapsulation and that there was a slight change in the size of the aggregates after drug encapsulation. In contrast, N-IMS-24/19 shows a substantial increase in R_h, from 2.4 nm to 21.6 nm post-encapsulation, suggesting transition from a single molecular state to aggregates upon drug encapsulation

In contrast, the autocorrelation patterns of N-IMS-22/53 and N-IMS-15/35 exhibited multi-exponential and irregular decay behaviors (Fig. 4d–e), reflecting a broader and multimodal particle size distribution, as observed in the intensity-based size distribution shown in Fig. S4. After encapsulation, these patterns smoothed, indicating a more uniform size distribution. From the number-based size distribution, the R_h values indicate the presence of single chains with R_h of 1.7 nm for N-IMS-22/53 and 1.1 nm for N-IMS-15/35 before encapsulation. After the encapsulation, the particle size increase to 14.2 nm (Table 3). Similarly, D-IMS-28.3/13/3 shows an initial single-chain R_h of 1.5 nm, which expands to 13.4 nm after encapsulation (Fig. 4f, Fig. S5, Table 3).

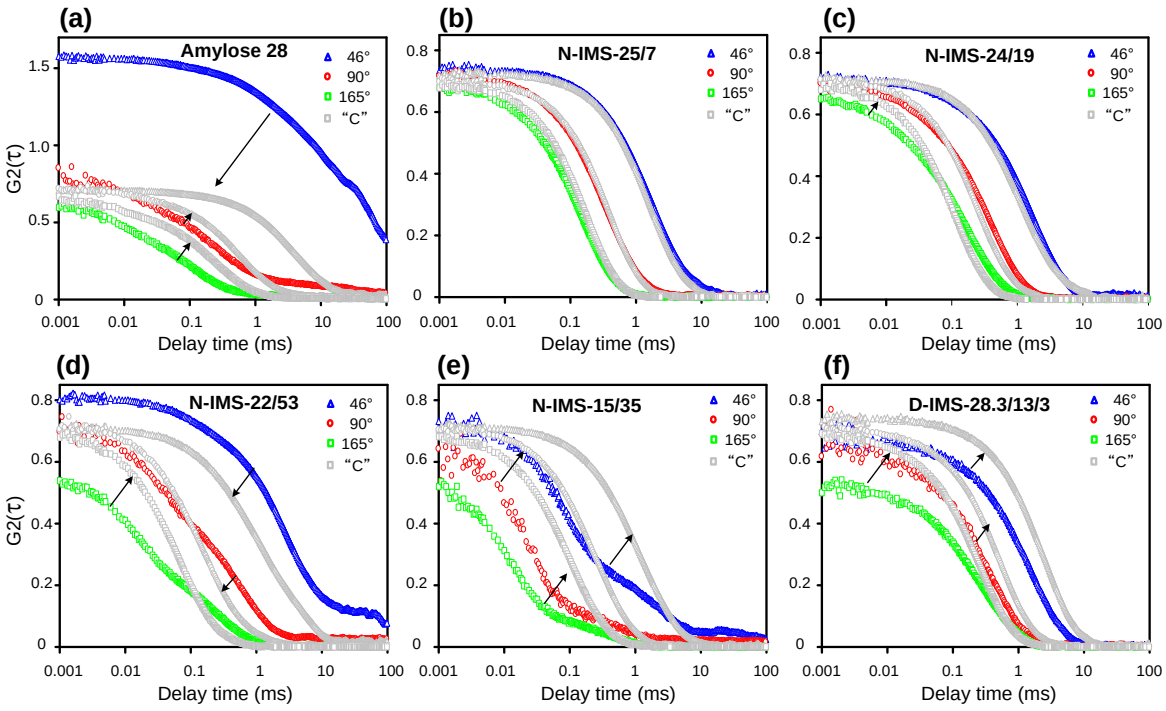

Fig. 4. Autocorrelation functions of intensity versus delay time at angles of 46°, 90°, and 165° for six pure sugars and their SZ-encapsulated samples prepared using method "C". Arrows indicate the transition direction from pure forms to complexed forms.

Table 3. Molecular characteristics of six sugar samples and their formed complexes with the SZ molecule in water at 25 °C.

Solution state	Samples	R_h [b]	R_g [c]	ρ [d]
Pure form	Amylose 28	1.4	1.52	1.09
	N-IMS-25/7	21.6	N/A	N/A
	N-IMS-24/19	2.4	2.97	1.24
	N-IMS-22/53	1.7	3.81	2.24
	N-IMS-15/35	1.1	4.04	3.67
	D-IMS-28.3/13/3	1.5	3.51	2.34
Complex "C" [a]	Amylose 28	18.0	1.74	0.10
	N-IMS-25/7	25.2	N/A	N/A
	N-IMS-24/19	21.6	N/A	N/A
	N-IMS-22/53	14.2	3.89	0.27
	N-IMS-15/35	14.2	3.73	0.26
	D-IMS-28.3/13/3	13.4	4.62	0.34

[a] Complex formed by method "C".

[b] R_h = hydrodynamic radius (nm) obtained from the average number-based particle size distribution using MADLS.

[c] R_g = Radius of gyration (nm) from SAXS.

N/A = not available due to significant aggregation (Table S1)

[d] Dimensionless $\rho = R_g/R_{h,}$ further discussed in Section 3.8

3.7. Structure analysis in water using SAXS. To gain a more detailed understanding of the morphology in water, SAXS analyses *via* Kratky plots [q^2I(q) versus q] and Guinier analysis [ln(I(q) versus q^2] were conducted in addition to the DLS analysis. Previously, only D-IMS-28.3/13/3 has been characterized in complex with ibuprofen (Lang et al., 2023a). The SAXS profile of D-IMS-28.3/13/3 showed a slight increase in intensity in the low q region and a downturn at higher q values. The Kratky plots revealed no difference in the high q region but increased intensity in the low q region upon complexation, suggesting that while the overall conformation remained unchanged, some chain aggregation occurred. The previously estimated R_g value of 2.4 nm was smaller than that in the current study's 3.51 nm (Table 3), possibly because aggregation progressed over time after sample preparation.

The SAXS profile of amylose 28 exhibited a pronounced upturn in the small q region, as shown in Fig. 5a, which was also subtly evident in the Kratky plot (Fig. 5b), indicating the presence of large-scale aggregation. Interestingly, a crystalline diffraction peak appeared at approximately 4 nm^{-1}, corresponding to a 2θ value of 5.7° (with $\lambda = 0.154$ nm), which converts to a q-value of 4.05 nm^{-1} (Section 2.4.2). This confirms the partial aggregation through crystallization. However, such an aggregation should be a minor component of the system, as discussed in the previous section. The Guinier plot analysis yielding a straight line depicted in Fig. 5c, with its gentle linear slope, suggests a small R_g of 1.52 nm (Table 3).

In contrast, N-IMS-25/7, in the smaller q region, displays a significant upturn behavior, yet the pattern differed markedly from that of amylose 28. The Kratky plot for this sample showed a distinct upturn curve in a different q region than that of amylose 28, a pattern not observed in other sugar samples, including N-IMS-24/19. The DLS results identified an aggregation with R_h of 21.6 nm as the main component, and the SAXS profile seemed to reflect this fact. N-IMS-25/7, characterized by the high α-(1→4)-linkage chain content, also exhibited the amylose crystalline peak at 4.0 nm^{-1} in solution. These results indicate that N-IMS-25/7 forms aggregates with crystalline core of N-4S and α-(1→6)-linkage chains radiating outward (Scheme 2a). The appearance of a 2θ value at 5.7° (approximately $q = 4$ nm^{-1}) in solution identifies the crystalline polymorph as a B-type crystal, consistent with the WAXS results obtained from the bulk state. The aggregate size was too large for observation within this SAXS range; hence, R_g was not determined because the complete Guinier region was not captured within the measured q-range (Tables 3 and S1).

N-IMS-24/19 exhibited a less pronounced aggregation, as evidenced by the lack of an upturn in the Kratky plot at low angles. This could be attributed to its extended α-(1→6)-glucosyl chain, which may reduce the association between N-4S segments.

As shown in Fig. 5d–e, N-IMS-15/35 and N-IMS 22/53 do not exhibit any aggregate pattern, and their scattering and Kratky plot profiles resemble those of flexible linear α-(1→6)-oligosaccharides with DPs of 7–11 (Suzuki et al., 2014). Both samples display an R_g range of 3.81–4.04 nm, which is larger than that of amylose 28 (Table 3).

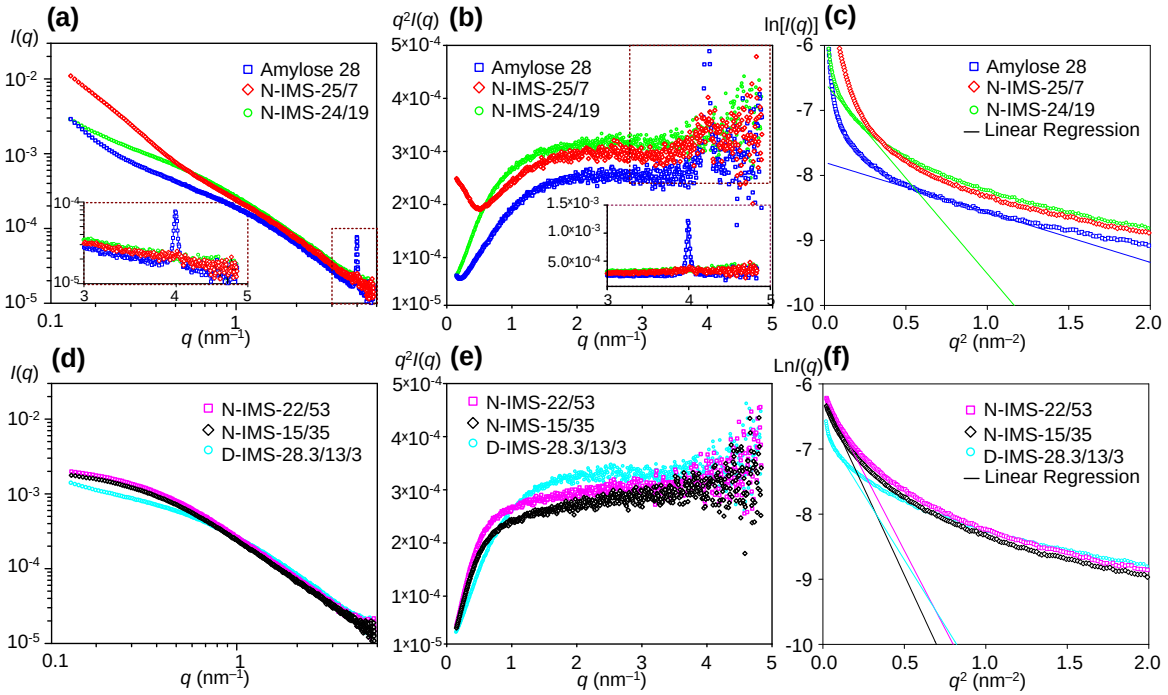

Fig. 5. SAXS profiles of (a) amylose 28, N-IMS-25/7, and N-IMS-24/19 are presented along with their Kratky plots in (b) and Guinier plots in (c). The inset in (a) and (b) shows an enlarged scale of the q region from 3–5 nm^{-1}, where the crystalline peak of amylose is evident. It is noted that the Guinier region of N-IMS-25/7 was absent in (c) because the $q_{max}R_g$ approximation exceeds 1.3. A similar order is observed in the second row for the SAXS profiles of (d) N-IMS-22/53, N-IMS-15/35, and D-IMS-28.3/13/3, accompanied by their Kratky plots in (e) and Guinier plots in (f).

The SAXS analysis for SZ complex "C" and "S" shows markedly distinct characteristics across samples enriched with α-(1→4)-linkages (Fig. 6). Amylose 28 showed much less upturn behavior in the low q region upon drug encapsulation using method "C", compared to method "S" (Fig. 6a). In addition, the crystalline peak became less pronounced, even disappearing (Fig. 6a, b). This behavior was attributed to the formation of fewer crystalline aggregates compared to that of pure amylose 28 due to interactions with the encapsulated drug. The R_g increases slightly from 1.52 to 1.74 nm with complexation using method "C" (Table 3).

548 In contrast, as shown in Fig. 6d and e, the upturn behavior was more pronounced for N-IMS-
549 25/7 after encapsulation with method "C," indicating enhanced aggregation and the slope
550 determination by Guinier analysis still failed (Fig. 6f). N-IMS-24/19, which was identified with
551 negligible aggregation from the DLS results in its pure form, seems to form a larger aggregate
552 structure after encapsulation with method "C" (Fig. 6g, h).
553 The samples with enriched α-(1→6)-linkages, N-IMS-22/53 and N-IMS-15/35, appear in a
554 similar scattering pattern and Kratky plot (Fig. 7). Upon drug encapsulation, the intensity of the
555 Kratky plot showed more pronounced changes for N-IMS-15/35 (Fig. 7e). Despite no observed
556 changes in R_g, R_h increased significantly (Fig. S5). The extent of aggregation and its structural
557 implications can be quantified by the dimensionless parameter ρ (R_g/R_h, Table 3). For example,
558 lentinan shows ρ = 3.23 as a single flexible chain in DMSO and ρ = 0.766 in ordered aggregates
559 (Zhang et al., 2010). Similarly, for most of the pure sugars including amylose 28, ρ exceeds 1,
560 signifying a well-swollen random coil chain structure. After encapsulation, ρ drops below 1,
561 indicating the high segment concentration in the aggregates, most likely due to the tightly packed α-
562 (1→4) segment core. For example, the ρ values for N-IMS-15/35 before and after drug encapsulation
563 were 3.67 and 0.26, respectively.
564 D-IMS complexed with SZ showed a pattern similar to that of IBP, where R_g was slightly
565 larger than that of the pure sample (Table 3).

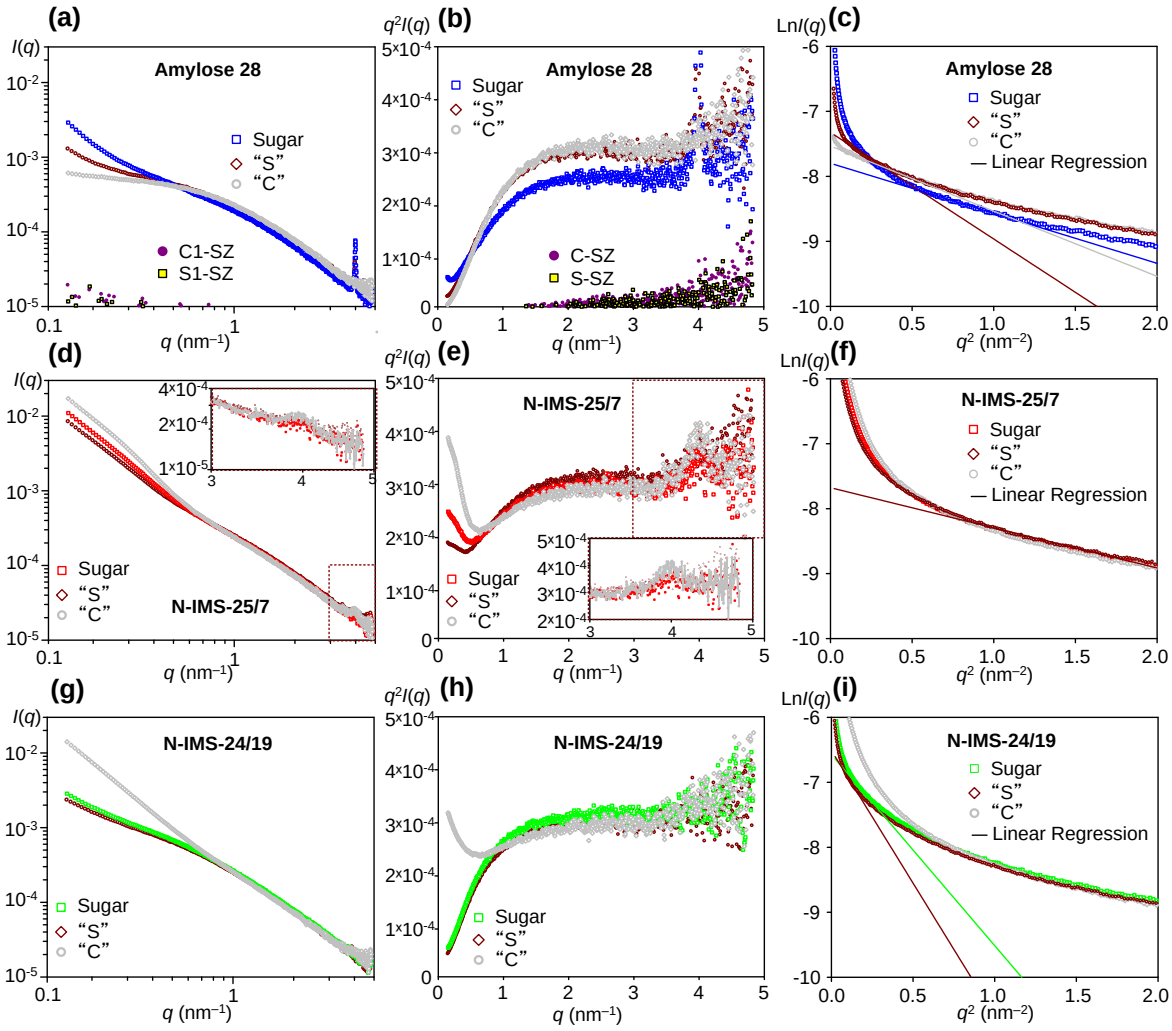

Fig. 6. SAXS profiles of pure sugar samples and their SZ-encapsulated forms prepared by methods "C" and "S": (a) Amylose 28, with corresponding Kratky plots in (b) and Guinier plots in (c). The second and third rows display similar data for N-IMS-25/7 and N-IMS-24/19, respectively. The inset in (d) and (e) shows an enlarged scale of the q region from 3–5 nm^{-1}, where the crystalline peak of N-IMS-25/7 is evident. Note that the Guinier region is absent for pure N-IMS-25/7 and its "C" complex in (f), as well as for the N-IMS-24/19 "C" complex in (i), due to the $q_{max}R_g$ approximation exceeding 1.3. SZ profiles from methods "C" and "S" are provided in (a) and (b) for reference.

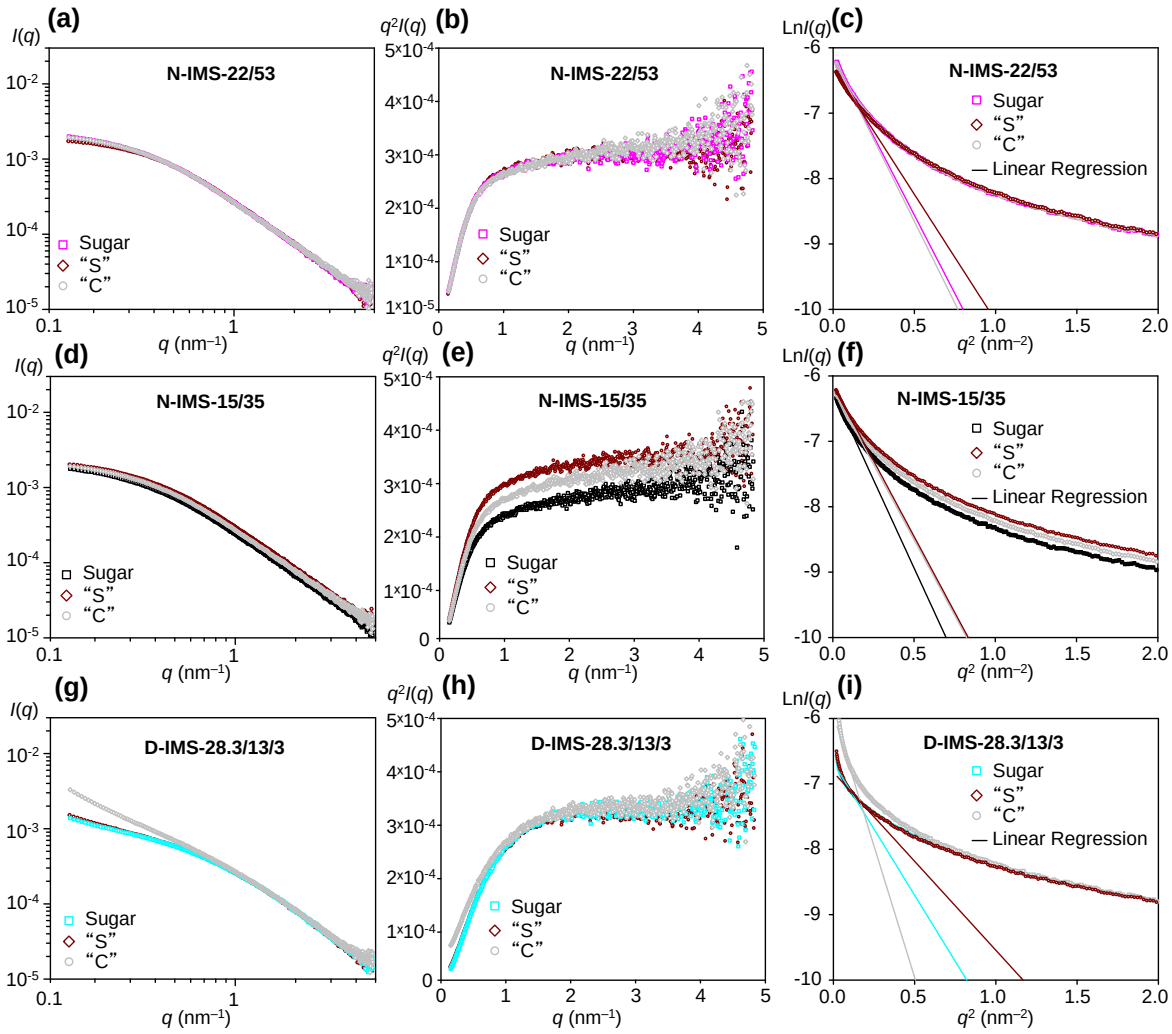

Fig. 7. SAXS profiles of pure sugar samples and their SZ-encapsulated forms prepared by methods "C" and "S": (a) N-IMS-22/53, with corresponding Kratky plots in (b) and Guinier plots in (c). The second and third rows display similar data for N-IMS-15/35 and D-IMS-28.3/13/3, respectively.

Altogether, we categorized the single chain as a molecularly dissolved chain with R_h of approximately 1.5 nm, as observed in number-based DLS. The morphologies with an R_h of 20 nm or lesser should be categorized as clusters composed of multiple sugar molecules, featuring a core of α-(1→4)-segment that is either in a hexagonally packed double helix crystalline state or in an amorphous state (Scheme 2a). This does not result in an upturn in the low q region of SAXS. Such a structure is dominant when interacting with SZ molecules. The larger aggregates, exceeding 100 nm as detected in intensity-based DLS, likely formed through further association of the 20 nm structures or uncontrolled retrogradation, which would account for the upturn in the low q region of SAXS.

Overall, while all samples formed B-type crystalline structures in bulk, the variations in the aggregation behavior in solution suggested differences in the interaction and organization of the crystalline regions at the nanoscale. The short α-(1→6) segments contribute to crystalline orderliness,

while longer segments enhance the chain and reduce large aggregate formation and precipitation (Scheme 2b). This study highlights the intricate relationship between crystalline structure and molecular dynamics in solution, particularly the role of the α-(1→6)-glucosyl chain in encapsulating large drug molecules. Despite these findings, the mechanism of SZ encapsulation and its location within the B-type crystal remains unclear, necessitating further research. Some potential limitations and ideas for future work include the limited range of hydrophobic drugs studied, which may restrict the generalizability of the results. Future studies could explore a broader spectrum of hydrophobic compounds to better understand how different molecular structures influence complex formation and drug release profiles. Additionally, while this study emphasizes crystalline patterns, it could benefit from examining the flexibility and conformational changes of the sugar chains in response to environmental factors, such as pH and ionic strength, and how these factors affect the aggregation behavior of these complexes. Understanding these dynamics will further enhance the design of effective drug delivery systems that respond to physiological conditions.

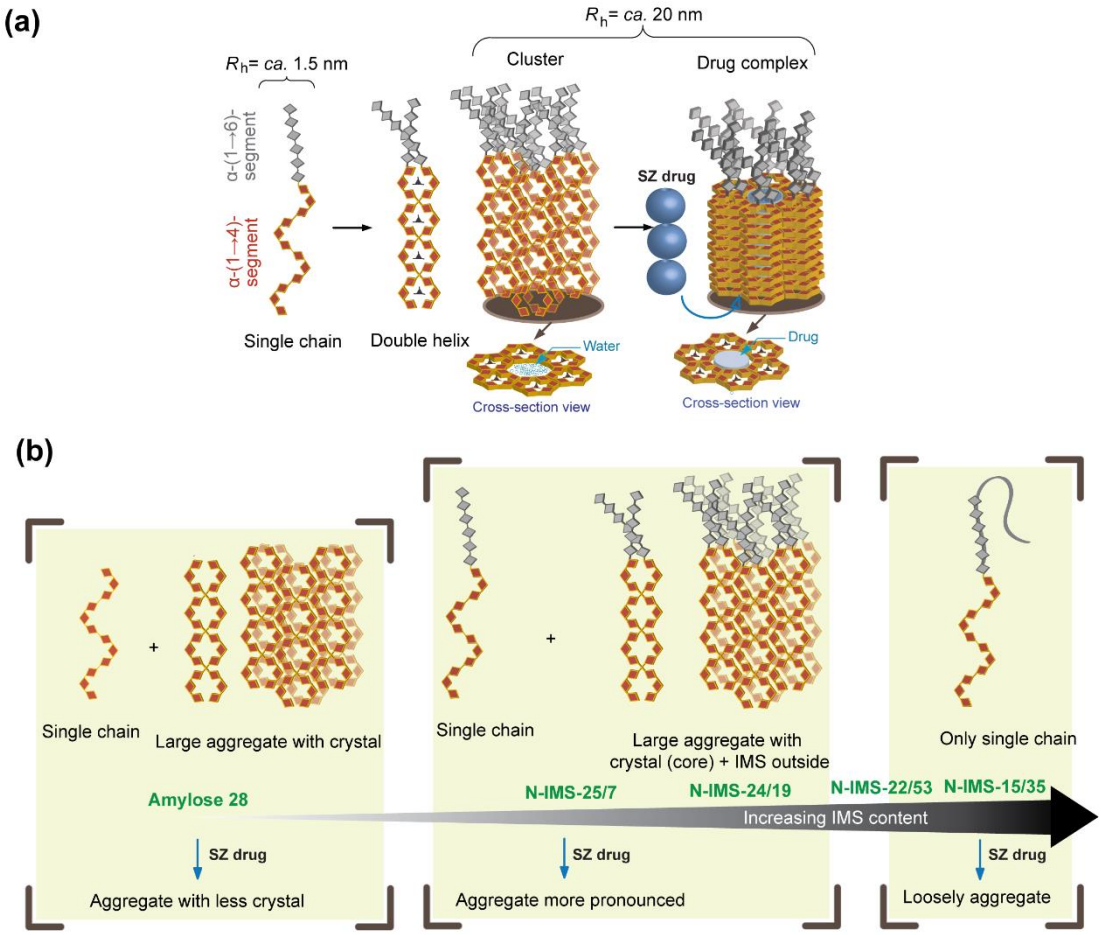

Scheme2. Conceptual models illustrating the proposed packing in solution for a single chain and aggregates of a hexagonal unit cell of chimeric IMS related to the B type polymorph. (a) The left-handed, parallel-stranded double helices curl in a parallel direction, leaving no space for water

molecules to enter. The packing arrangement of the double helices (cylinders) forms clusters, featuring a large channel centered around the sixfold screw axis, theoretically accommodating up to 36 water molecules. However, the large-size drug (SZ, sulfasalazine) of three aromatic benzene rings and steric hindrance with polar sulfate and carboxylic groups, might prevent it from occupying a single cavity to form a V-type polymorph, allowing only partial incorporation into the B-type amorphous regions. (b) Aggregation patterns of short amylose and four N-IMS samples, both before and after drug encapsulation. Drug-induced aggregation is triggered by interactions with the N-4S chains, promoting the formation of larger aggregates.

4. Conclusion

This study investigated the structure of a novel linear glucoconjugate formed between amylose and dextran, emphasizing the structural interactions between N-IMS and D-IMS samples synthesized enzymatically. The short amylose chains (N-4S) aligned effectively, forming a B-type crystal structure. Correlating the MADLS and SAXS results for both the pure sugars and their freeze-thawed complexes with the hydrophobic drug SZ provided valuable insights into the dimensional features of various morphologies in water. Among the samples, N-IMS-25/7 demonstrated the highest drug-binding capacity, forming a rigid core most likely with a B-type structure. The N-IMS-24/19 complex displayed similar characteristics after drug encapsulation. These findings not only contribute to the fundamental understanding of glucoconjugate behavior but also underscore the potential of carbohydrate polymers in drug delivery systems. Future research should explore the molecular patterns of chimeric IMSs with different drug structures to gain a deeper understanding of their interactions and encapsulation mechanisms. Such insights will be critical for designing more effective drug delivery systems, enabling targeted therapy and controlled release, and ultimately enhancing therapeutic efficacy. The implications of this work extend beyond this study, offering a pathway for the development of innovative carbohydrate-based carriers in pharmaceutical applications.

Data availability

All data supporting the findings of this study are available from the first author (W. Lang) upon reasonable request.

CRediT authorship contribution statement

Weeranuch Lang: Conceptualization, investigation, formal analysis, writing–original draft, review, and editing. Yoshiaki Yuguchi: Formal analysis, writing, review, and editing. Chun-Yao Ke, Ting-Wei Chang, Yuya Kumagai, Wilaiwan Kaenying: Formal analysis. Takayoshi Tagami, Feng Li, Takuya Yamamoto, Kenji Tajima, and Toshifumi Satoh: Resources and supervision. Kenji Takahashi:

Funding acquisition and supervision. Takuya Isono: Funding acquisition, conceptualization, supervision, review, and editing. Atsuo Kimura: Supervision, project administration, writing, review, and editing.

Acknowledgement

The synchrotron radiation experiments were performed at the Photon Factory (proposal numbers 2023G574 and 2024G113). This study was partially supported by the Program for the Promotion of Basic and Applied Research for Innovations in Bio-oriented Industry (BRAIN), Japan [Grant numbers 25001A and 26062B], and the Japan Society for the Promotion of Science KAKENHI [Grant numbers 17H03801 and 19KK0147]. Part of this study was supported by JST COI-NEXT (no. JPMJPF2102) and JST PREST (no. JPMJPR23N2), and JST ASPIRE for Rising Scientists (no. JPMJAP2333). We thank Editage (www.editage.jp) for English language editing.

Declaration of competing interest

The authors declare that they have no competing financial interests or personal relationships that may have influenced the work reported in this study.

References

Bertoft, E. (2017). Understanding starch structure: Recent progress. Agronomy, 7, 56. https://doi.org/10.3390/agronomy7030056

Braga, D., Ferracini, E., Ferrero, A., Ripamonti, A., Brant, D. A., Buliga, G. S., & Cesàro, A. (1985). Amylose conformation in aqueous solution: A small-angle X-ray scattering study. International Journal of Biological Macromolecules, 7, 161–166. https://doi.org/https://doi.org/10.1016/0141-8130(85)90019-4

Breitinger, H. G. (2003). Synthesis and characterization of 2,3-di-*O*-alkylated amyloses: Hydrophobic substitution destabilizes helical conformation. Biopolymers, 69, 301–310. https://doi.org/10.1002/bip.10384.

Dıblan, S., Salum, P., Ulusal, F., & Erbay, Z. (2024). Impact of conjugation of whey protein concentrate with different carbohydrates: Monitoring structural and technofunctional variations. International Dairy Journal, 158, 106036. doi:10.1016/j.idairyj.2024.106036.

Frost, K., Kaminski, D., Kirwan, G., Lascaris, E., & Shanks, R. (2009). Crystallinity and structure of starch using wide angle X-ray scattering. Carbohydrate Polymers, 78, 543–548. doi:10.1016/j.carbpol.2009.05.018.

Hara, H., Kume, S., Iizuka, T., Fujimoto, Y., & Kimura, A. (2017). Enzymatically synthesized megalo-type isomaltosaccharides enhance the barrier function of the tight junction in the intestinal epithelium. Bioscience, Biotechnology and Biochemistry, *82*(4), 629–635.

https://doi.org/10.1080/09168451.2017.1398065
Higuchi, T., & Connors, A. (1965). Phase-solubility techniques. In C. N. Reilly (Ed.). Advances in analytical chemistry instrumentation, 4 (pp. 117–212). New York, NY: Interscience, 4.
Hu, Q., Lu, Y., & Luo, Y. (2021). Recent advances in dextran-based drug delivery systems: From fabrication strategies to applications. Carbohydrate Polymers, 264, 117999. doi:10.1016/j.carbpol.2021.117999.
Imberty, A., De Recherche, C., & Perez, S. (1988). A revisit to the three-dimensional structure of B-type starch. Biopolymers, 27, 1205–1221. doi:10.1002/bip.360270803.
Kimura, A., Hara, H., & Lang, W. (2015). Production methods and application of isomaltomegalosaccharides having double- or single-anchor and use thereof. Japan Patent no. 6655246B2.
Lang, W., Sirisansaneeyakul, S., Ngiwsara, L., Mendes, S., Martins, L. O., Okuyama, M., & Kimura, A. (2013). Characterization of a new oxygen-insensitive azoreductase from *Brevibacillus laterosporus* TISTR1911: Toward dye decolorization using a packed-bed metal affinity reactor. Bioresource Technology, 150, 298–306. doi:10.1016/j.biortech.2013.09.124.
Lang, W., Kumagai, Y., Sadahiro, J., Maneesan, J., Okuyama, M., Mori, H., Sakairi, N., & Kimura, A. (2014). Different molecular complexity of linear-isomaltomegalosaccharides and β-cyclodextrin on enhancing solubility of azo dye ethyl red: Towards dye biodegradation. Bioresource Technology, 169, 518–524. https://doi.org/10.1016/j.biortech.2014.07.025
Lang, W., Kumagai, Y., Sadahiro, J., Saburi, W., Sarnthima, R., Tagami, T., Okuyama, M., Mori, H., Sakairi, N., Kim, D., & Kimura, A. (2022a). A practical approach to producing isomaltomegalosaccharide using dextran dextrinase from *Gluconobater oxydans* ATCC 11894. Applied Microbiology and Biotechnology, 106, 689–698. https://doi.org/10.1007/s00253-021-11753-6
Lang, W., Kumagai, Y., Habu, S., Sadahiro, J., Tagami, T., Okuyama, M., Kitamura, S., Sakairi, N., & Kimura, A. (2022b). Physicochemical functionality of chimeric isomaltomegalosaccharides with α-(1 → 4)-glucosidic segments of various lengths. Carbohydrate Polymers, 291, 119562. https://doi.org/10.1016/j.carbpol.2022.119562
Lang, W., Tagami, T., Kumagai, Y., Tanaka, S., Kang, H. J., Okuyama, M., Kimura, A. (2023a). Tunable structure of chimeric isomaltomegalosaccharides with double α-(1 → 4)-glucosyl chains enhances the solubility of water-insoluble bioactive compounds. Carbohydrate Polymers, 319, 121185. doi:10.1016/j.carbpol.2023.121185.
Lang, W., Sirisansaneeyakul, S., Tagami, T., Kang, H. J., Okuyama, M., Sakairi, N., & Kimura, A. (2023b). Nonreducing terminal chimeric isomaltomegalosaccharide and its integration with azoreductase for the remediation of soil-contaminated lipophilic azo dyes. Carbohydrate Polymers, 305, 120565. doi:10.1016/j.carbpol.2023.120565.

Lasemi, N., Rupprechter, G., Liedl, G., & Eder, D. (2021). Near-infrared femtosecond laser ablation of Au-coated Ni: Effect of organic fluids and water on crater morphology, ablation efficiency and hydrodynamic properties of NiAu nanoparticles. Materials, 14, 5544. doi:10.3390/ma14195544.

Naknean, P., & Meenune, M. (2010). Review article. Factors affecting retention and release of flavour compounds in food carbohydrates. International Food Research Journal, 34, 23–34.

Nielsen. T. and T., Wintgens p. V., Amiel, C., Wimmer, R., & Larsen, K. L. (2010). Facile synthesis of β-cyclodextrin-dextran polymers by "click" chemistry. Biomacromolecules, 11, 1710–1715. https://doi.org/10.1021/bm9013233.

Nishimura, T., & Akiyoshi, K. (2017). Amylose engineering: Phosphorylase-catalyzed polymerization of functional saccharide primers for glycobiomaterials. Wiley Interdisciplinary Reviews. Nanomedicine and Nanobiotechnology, 9, 1–15. doi:10.1002/wnan.1423.

Pfannemüller, B. (1987). Influence of chain length of short monodisperse amyloses on the formation of A- and B-type X-ray diffraction patterns. International Journal of Biological Macromolecules, 9, 105–108. doi:10.1016/0141-8130(87)90034-1.

Pluemsab, W., Sakairi, N., & Furuike, T. (2005). Synthesis and inclusion property of α-cyclodextrin-linked alginate. Polymer, 46, 9778–9783. doi:10.1016/j.polymer.2005.08.005.

Ramirez, H. L., Valdivia, A., Cao, R., Fragoso, A., Torres Labandeira, J. J., Baños, M., & Villalonga, R. (2007). Preparation of β-cyclodextrin-dextran polymers and their use as supramolecular carrier systems for naproxen. Polymer Bulletin, 59, 597–605. doi:10.1007/s00289-007-0803-8.

Sahu, K. M., Patra, S., & Swain, S. K. (2023). Host-guest drug delivery by β-cyclodextrin assisted polysaccharide vehicles: A review. International Journal of Biological Macromolecules, 240(October 2022), 124338. doi:10.1016/j.ijbiomac.2023.124338.

Sun, X., Sun, Z., Saleh, A. S. M., Zhao, K., Ge, X., Shen, H., Li, W. (2021). Understanding the granule, growth ring, blocklets, crystalline and molecular structure of normal and waxy wheat A- and B- starch granules. Food Hydrocolloids, 121, 107034. doi:10.1016/j.foodhyd.2021.107034.

Sundari, C. S., & Balasubramanian, D. (1997). Hydrophobic surfaces in saccharide chains. Progress in Biophysics and Molecular Biology, 67, 183–216. doi:10.1016/s0079-6107(97)00016-3.

Surendren, A., Mohanty, A. K., Liu, Q., & Misra, M. (2022). A review of biodegradable thermoplastic starches, their blends and composites: Recent developments and opportunities for single-use plastic packaging alternatives. Green Chemistry, 24, 8606–8636. doi:10.1039/D2GC02169B.

751 Suzuki, S., Yukiyama, T., Ishikawa, A., Yuguchi, Y., Funane, K., & Kitamura, S. (2014).
752 Conformation and physical properties of cycloisomaltooligosaccharides in aqueous solution.
753 Carbohydrate Polymers, 99, 432–437. doi:10.1016/j.carbpol.2013.07.089.
754 Tahir, M. N., Cao, Y., Azzouz, A., & Roy, R. (2021). Host-guest chemistry of the sulfasalazine-β-
755 cyclodextrin inclusion complex. Tetrahedron, 85, 132052. doi:10.1016/j.tet.2021.132052.
756 Tao, F., & Bernasek, S. L. (2005). Two-dimensional self-assembly of a two-component molecular
757 system: Formation of an ordered and homogeneous molecular mesh. Journal of the American
758 Chemical Society, 127, 12750–12751. doi:10.1021/ja050365p.
759 Wang, Y., Zhang, Y., Guan, L., Wang, S., Zhang, J., Tan, L., Zhang, H. (2021). Lipophilization
760 and amylose inclusion complexation enhance the stability and release of catechin.
761 Carbohydrate Polymers, 269, 118251. doi:10.1016/j.carbpol.2021.118251.
762 Wintgens, V., Lorthioir, C., Dubot, P., Sébille, B., & Amiel, C. (2015). Cyclodextrin/dextran based
763 hydrogels prepared by cross-linking with sodium trimetaphosphate. Carbohydrate Polymers,
764 *132*, 80–88. doi:10.1016/j.carbpol.2015.06.038.
765 Yamamoto, K., Yoshikawa, K., & Okada, S. (1993). Effective dextran production from starch by
766 dextrin dextranase with debranching enzyme. Journal of Fermentation and Bioengineering,
767 76, 411–413. doi:10.1016/0922-338X(93)90035-7.
768 Yang, L., Zhang, B., Yi, J., Liang, J., Liu, Y., & Zhang, L. M. (2013). Preparation, characterization,
769 and properties of amylose-ibuprofen inclusion complexes. Starch – Stärke, 65, 593–602.
770 doi:10.1002/star.201200161.
771 Yang, Z., Swedlund, P., Hemar, Y., Mo, G., Wei, Y., Li, Z., & Wu, Z. (2016). Effect of high
772 hydrostatic pressure on the supramolecular structure of corn starch with different amylose
773 contents. International Journal of Biological Macromolecules, 85, 604–614.
774 doi:10.1016/j.ijbiomac.2016.01.018.
775 Zhang, Y., Li, S., & Zhang, L. (2010). Aggregation behavior of triple helical polysaccharide with
776 low molecular weight in diluted aqueous solution. Journal of Physical Chemistry. B, 114,
777 4945–4954. doi:10.1021/jp9100398.
778 Zhang, Y., Zhu, Y., Ma, P., Wu, H., Xiao, D., Zhang, Y. (2023). Functional carbohydrate-based
779 hydrogels for diabetic wound therapy. Carbohydrate Polymers, 312, 120823.
780 doi:10.1016/j.carbpol.2023.120823
781 Zitting, A., Paajane, A., & Penttilä, P. A. (2023). Impact of hemicelluloses and crystal size
782 on X-ray scattering from atomistic models of cellulose microfibrils. *Cellulose*, *30*, 8107–
783 8126. https://doi.org/10.1007/s10570-023-05357-8
784